Advanced Powder Technology 28 (2017) 385–397

Contents lists available at ScienceDirect

Advanced Powder Technology

journal homepage: www.elsevier.com/locate/apt

Original Research Paper

Phase-change heat transfer of single/hybrid nanoparticles-enhanced phase-change materials over a heated horizontal cylinder confined in a square cavity

A.J. Chamkha [a,b], A. Doostanidezfuli [c], E. Izadpanahi [d], M. Ghalambaz [c,*]

[a] Mechanical Engineering Department, Prince Mohammad Bin Fahd University, Al-Khobar 31952, Saudi Arabia
[b] Prince Sultan Endowment for Energy and Environment, Prince Mohammad Bin Fahd University, Al-Khobar 31952, Saudi Arabia
[c] Department of Mechanical Engineering, Dezful Branch, Islamic Azad University, Dezful, Iran
[d] Department of Mechanical and Materials Engineering, Florida International University, Miami, FL 33199, United States

ARTICLE INFO

Article history:
Received 25 July 2016
Received in revised form 25 September 2016
Accepted 9 October 2016
Available online 26 October 2016

Keywords:
Hybrid nanofluid
Laminar natural convection
Phase-change heat transfer
Melting in cavity

ABSTRACT

The melting process of a nano-enhanced phase-change material is investigated in a square cavity with a hot cylinder located in the middle of the cavity in the presence of both single and hybrid nanoparticles. The dimensionless partial differential equations are solved numerically using the Galerkin finite element method using a grid with 6000 quadrilateral elements. The effects of the volume fraction of nanoparticles, the Fourier number, the thermal conductivity parameter, and the viscosity parameters are studied. The results show that the solid-liquid interface and the liquid fraction are significantly affected by the volume fraction of nanoparticles and the thermal conductivity parameter. Additionally, it is found that the melting rate is much larger when the Fourier number changes between 0 and 0.5 and a further increase in the Fourier number causes a reduction in the rate of the melting.

1. Introduction

Natural convection caused by a circular cylinder inside an enclosure has a variety of applications in engineering systems such as compact heat exchangers, solar collectors, cooling of electronic devices, chemical reactors. Cesini et al. [1] conducted a numerical and experimental study of the natural convection induced by a horizontal cylinder in a rectangular cavity. Yoon et al. [2] reported the natural convection results from two hot circular cylinders inside a cavity. They found that the bifurcation from steady state to unsteady state natural convection significantly depends on the location of the inner cylinders and the Rayleigh number. Huang et al. [3] investigated the natural convection caused by a time-periodic pulsating temperature of a cylinder inside a square cavity. They reported an enhancement in the heat transfer compared to the steady state natural convection. Zhang et al. [4] numerically studied the effects of an elliptic cylinder on the natural convection inside a square cavity using the Galerkin method.

One of the reliable ways of storing energy is using Phase Change Materials (PCMs). This is due to the fact that a small volume of PCMs can store a substantial amount of energy during the phase-change process. The phase-change materials are now widely used in a variety of applications such as cooling of electronic devices [5] in various fields of thermal management of high power electronics [6], cooling of mobile electronic devices [7], cooling enhanced by heat pipes [8]. An excellent review on thermal management systems using phase-change materials for electronic components has been reported by Ziye et al. [9]. The phase-change materials have also found important applications in solar heating systems [6,9]. An extensive review of the applications of phase-change materials has been addressed by Sharif et al. [10]. Also, PCMs have been utilized in waste heat recovery systems [11].

Despite the fact that the phase-change materials are now widely used in a variety of applications, they have a weak thermal conductivity causing a reduction in the performance of the energy storage unit. Luckily, the thermal conductivity of the PCMs can be enhanced using nanofluids. Zeng et al. [12] reported an enhancement in the thermal conductivity of a composite PCM using Ag nanoparticles. A significant augmentation in the thermal conductivity of PCMs was reported by Liu et al. [13] by utilizing a small volume fraction of TiO_2 nanoparticles in saturated $BaCl_2$. Wu

* Corresponding author.
E-mail addresses: achamkha@pmu.edu.sa (A.J. Chamkha), doostaniali@gmail.com (A. Doostanidezfuli), eizad001@fiu.edu (E. Izadpanahi), m.ghalambaz@iaud.ac.ir (M. Ghalambaz).

http://dx.doi.org/10.1016/j.apt.2016.10.009
0921-8831/

Nomenclature

$S(T)$	Carman-Kozeny equation (source term)
A_{mush}	mushy-zone constant (Carman-Koseny equation constant)
C	specific heat (J/kg K)
C_p	specific heat in constant pressure (J/kg K)
D	diameter of the cylinder
R	radius of the cylinder
g	gravity (m/s^2)
k	thermal conductivity (W/m K)
L	latent heat of fusion (J/kg)
P	pressure (Pa)
S	enclosure inclination angle
T	temperature (K)
t	time (s)
H	length and Height (m)
u	velocity in the x-direction (m/s)
v	velocity in the y-direction (m/s)
T_f	melting temperature (K)
Ra	Rayleigh number
Pr	Prandtl number
Ste	Stefan number
Nc	conductivity parameter
Nv	viscosity parameter
x, y	Cartesian coordinates

Greek symbols

φ (T)	liquid fraction
α	thermal diffusivity (m^2/s)
ϕ	volume fraction of nanoparticles
μ	dynamic Viscosity (kg/m s)
ρ	density (kg/m^3)
ε	Carman-Kozeny equation constant
υ	kinematic viscosity (m^2/s)
ΔT	mushy-zone temperature range (K)
ξ	basis functions
γ	the ratio of thermal diffusivity
β	thermal expansion coefficient (1/K)
θ	non-dimensional temperature

Subscripts

F	fusion
l	liquid phase
s	solid phase
hnf	hybrid nanofluid
nf	nanofluid
bf	base fluid
p	particles
h	hot
i	interface position
c	cold
k	node number
i	residual number

et al. [14] found that the heating and cooling times declines up to 30.3% and 28.2% exploiting 1% of Cu nanoparticles in paraffin. Harikrishnan and Kalaiselvam [15] reported a reduction up to 27.67% and 28.57% in the solidification and melting time using CuO in oleic phase-change material. The nanofluids in liquid form have also been studied in many recent studies. For instance, different heat transfer aspects of nanofluids including mixed convection in micro channels [16], film condensation [17] and the effect of magnetic fields on the heat transfer of nanofluid [18,19] and natural convection in enclosures [19,20] and non-Newtonian nanofluids [21].

The aforementioned studies have been done utilizing a single metallic or non-metallic nanoparticles. The metallic nanoparticles are known for their high thermal conductivity, however, their tendency to chemical reactions make them an unreliable choice. On the other hand, the non-metallic particles have a high stability and chemical inertness, albeit, they possess a weak thermal conductivity. Recently, it is suggested to combine a small amount of metallic nanoparticles with non-metallic nanoparticles causing an enhancement in the thermal properties of the base fluid. Suresh et al. [22] reported a considerably higher augmentation in the viscosity compared to the thermal conductivity using Al_2O_3–Cu hybrid nanoparticles. Suresh et al. [23] reported a maximum enhancement of 13.56% in the Nusselt number by using an Al_2O_3–Cu hybrid nanofluid. Yarmand et al. [24] reported a maximum 32.7% enhancement in the values of the Nusselt number using a GNP–Ag/water hybrid nanofluid. Takabi and Salehi [25] numerically investigated the effects of Al_2O_3–Cu/water hybrid nanofluids inside a sinusoidal corrugated enclosure. They reported higher enhancement in the heat transfer rate using a hybrid nanofluid compared to a regular nanofluid. Takabi and Shokouhmand [26] numerically studied the effects of an Al_2O_3–Cu/water hybrid nanofluid on the heat transfer rate in the turbulent regime. It was found that the hybrid nanofluid causes improvements in the heat transfer rate and also it has an undesirable effect on the friction factor which causes higher pressure drop in the hybrid nanofluid. The effects of Al_2O_3–Cu/water hybrid nanofluid over a stretching sheet was numerically investigated by Surya and Anjali [27]. It was shown that the Al_2O_3–Cu/water hybrid nanofluid has a higher heat transfer rate compared to the Cu/water nanofluid even in the presence of a magnetic field.

Due to the significant importance of phase-change materials and their applications in the energy storage systems and the fact that nano-enhanced phase-change materials could increase the performance of an energy storage system, the authors of the present study feel necessary to conduct the present research. In this paper, the effects of hybrid and single nanoparticles on the melting process of nano-enhanced phase-change materials are investigated inside a square cavity for the first time. The melting is caused by a hot cylinder located in the center of the cavity. The governing set of equations has been solved numerically using the Galerkin finite element method using 6000 quadrilateral elements. The results of the present study are compared with both experimental and numerical results available in the literature. The authors hope that the results of the present study could help to improve the design and the functionality of energy storage systems in the future. To the best of the authors' knowledge, the results of the present paper are unique and the authors hope that the results of this paper help to design much efficient energy storage systems in the future.

2. Geometric and mathematical models

2.1. Physics of the problem

As shown in Fig. 1, the schematic of a horizontal cylinder in a square cavity, A concentric heated circular cylinder of radius R

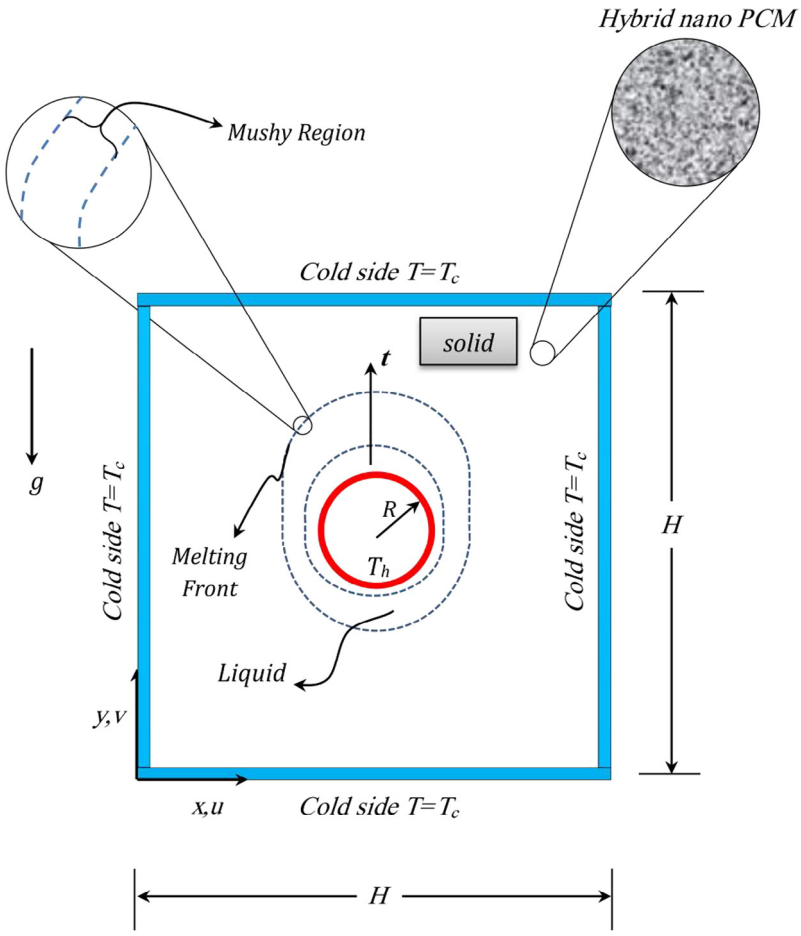

Fig. 1. A schematic view of geometry details and physical model.

located inside a cavity of height and width H. The cavity is filled with a nano-enhanced phase-change material including hybrid nanoparticles (HNePCM), the vertical and horizontal walls of the cavity are maintained at a uniform cold temperature T_c according to Fig. 1, consists of a cylinder (with diameter $D = 2R$) with a high temperature T_h. The area between the cylinder and the cavity is initially maintained at a uniform temperature T_c. A schematic view of the geometry details and the physical model are shown in Fig. 1. In addition, the following assumptions are made in present work.

The single/hybrid nanofluid shows a Newtonian behavior due to the fact that experimental data on the behavior of most of the nanofluids demonstrate that the regular nanofluids and hybrid nanofluids follow the Newtonian behavior [22,28,29]. The viscous dissipation and the thermal radiation are assumed negligible. This assumption is valid as the driving force for the liquid is the natural convection and the temperature differences in PCMs are limited. The base fluid and the nanoparticles are considered as continuous media and uniformly distributed as they are assumed to be in thermodynamic equilibrium. As for the preparation of the nanofluids, the ultrasonic techniques or stabilizers additives are utilized, the nanofluid could be assumed as a homogeneous suspension of nanoparticles and the base fluid. As discussed in the work of Buongiorno [30], the nanoparticles are very tiny, and hence, the Biot number of nanofluids is very small. Therefore, they can be assumed to be in thermal equilibrium with the base fluid. The applied temperature difference in the cavity is assumed to be limited, and hence, the Boussinesq approximation for the buoyancy force is utilized. As mentioned, the temperature difference for PCMs is small. There is no chemical reaction between different types of the nanoparticles and the base fluid. This assumption is valid because the nanoparticles are selected in a way that they are inherently inactive with the base fluid or with each other to gain a stable suspension. These mentioned assumptions are generally valid for many of single/hybrid nano-enhanced PCMs applications.

2.2. Governing equations

According to the physical model of the cavity with the hot inner cylinder, the governing partial differential equations can be written as follows:

Continuity

$$\nabla \cdot u = 0 \tag{1}$$

Momentum

$$\frac{\partial u}{\partial t} + (u \cdot \nabla)u = -\frac{1}{\rho_{hnf}}\nabla P + \frac{\mu_{hnf}}{\rho_{hnf}}\nabla \cdot (\mu(\varphi)\nabla u) + \frac{\beta_{hnf}}{\rho_{hnf}} g(T - T_f) + \frac{1}{\rho_{hnf}} S(T)u \tag{2}$$

Energy

$$\frac{\partial T}{\partial t} + (u) \cdot \nabla T = \alpha_{hnf}\nabla(\alpha_{hnf}(\varphi)\nabla T) - \frac{L}{(C_p)_{hnf}}\frac{\partial \varphi(T)}{\partial t} \tag{3}$$

The above equations in expanded form are as follows:

Here $\alpha(\varphi) = \alpha_{l,\ hnf}\varphi + \alpha_{s,\ hnf}(1 - \varphi)$ and φ is the melt fraction and can be measured utilizing the temperature as follows:

$$\varphi(T)=\begin{cases}0 & T<T_f\\ \frac{T-T_f}{\Delta T} & T_f<T<T_f+\frac{\Delta T}{2}\\ 1 & T>T_f+\Delta T\end{cases} \tag{4}$$

where ΔT represents the temperature of the mushy-zone. The viscosity of the mushy zine can also be controlled by the following relation:

$$\mu(\varphi)=\mu_l(1+A_{mush}(1-\varphi)) \tag{5}$$

Controlling the viscosity using Eq. (5) in the mushy region causes the pressure and the velocity fields to be uniform in the domain of the solution. Additionally, it causes the velocity field to be zero close to the solid parts of the domain. As mentioned, the thermal diffusivity in the liquid, mushy and solid regions is a linear function of the volume fraction of the liquid as $\alpha(\varphi)=\alpha_{l,\ hnf}\varphi+\alpha_{s,\ hnf}(1-\varphi)$. The source term $S(T)$ in the momentum equation is assumed to be a continuous equation for phase change by using the Carman-Kozeny equation as follow:

$$S(T)=-A_{mush}\frac{(1-\varphi(T))^2}{\varphi(T)^3+\varepsilon} \tag{6}$$

The buoyancy force which creates the motion in the liquid phase and causes the liquid to move upward and natural convection happens, is modeled by utilizing the Boussinesq approximation as follows:

$$\vec{F}=\rho_{hnf}\beta\vec{g}(T-T_f) \tag{7}$$

Based on the problem description and according to Fig. 1, the boundary conditions are given by:

On all externals walls of the cavity $T=T_c$ and $u=v=0$ (8a)

On the cylinder $T=T_h$ (8b)

Eqs. (4)–(7) are changed into the non-dimensional form by utilizing the following dimensionless variables:

$$X=\frac{x}{H},\quad Y=\frac{y}{H},\quad U=\frac{uH}{\alpha_{l,bf}},\quad V=\frac{vH}{\alpha_{l,bf}},\quad \theta=\frac{T-T_f}{T_h-T_f},\quad AR=\frac{R}{L} \tag{9a}$$

$$Fo=\frac{t\alpha_{bf}}{\mathrm{H}^2},\quad S(\theta)=\frac{s(T)\mathrm{H}^2}{\rho_{l,hnf}\alpha_{l,bf}},\quad \mu_r=\frac{\mu_{hnf}(\varphi)}{\mu_{bf}},\quad \alpha_r=\frac{\alpha_{hnf}(\varphi)}{\alpha_{bf}},$$
$$P=\frac{\mathrm{PH}^2}{\rho_{l,bf}\alpha_{l,bf}^2} \tag{9b}$$

Accordingly, the dimensionless parameters can be written as follows:

$$Ra=\frac{g\beta_{bf}(T_h-T_f)L^3}{\alpha_{l.bf}\upsilon_{bf}},\quad Ste=\frac{C_{l,bf}(T_h-T_f)}{L},\quad Pr=\frac{\upsilon_{bf}}{\alpha_{l,bf}} \tag{10}$$

Here *Ra*, *Ste*, and *Pr* represent the Rayleigh number, the Stefan number, and the Prandtl number, respectively. By substituting Eqs. (8) and (9) into Eqs. (1)–(3), the dimensionless form of the governing Eqs. (11)–(14) are derived as follows:

Continuity:

$$\frac{\partial U}{\partial X}+\frac{\partial V}{\partial Y}=0 \tag{11}$$

Momentum in *X*-direction:

$$\frac{\partial U}{\partial Fo}+U\frac{\partial U}{\partial X}+V\frac{\partial U}{\partial Y}=-\frac{\rho_{bf}}{\rho_{hnf}}\frac{\partial P}{\partial X}+\frac{\rho_{bf}}{\rho_{hnf}}\frac{\mu_{hnf}}{\mu_{bf}}Pr\left(\frac{\partial}{\partial X}\left(\mu_r\frac{\partial U}{\partial X}\right)+\frac{\partial}{\partial Y}\left(\mu_r\frac{\partial U}{\partial Y}\right)\right)+\frac{\rho_{bf}}{\rho_{hnf}}S(\theta)U \tag{12}$$

Momentum in *Y*-direction:

$$\frac{\partial V}{\partial Fo}+U\frac{\partial V}{\partial X}+V\frac{\partial V}{\partial Y}=-\frac{\rho_{bf}}{\rho_{hnf}}\frac{\partial P}{\partial Y}+\frac{\rho_{bf}}{\rho_{hnf}}\frac{\mu_{hnf}}{\mu_{bf}}Pr\left(\frac{\partial}{\partial X}\left(\mu_r\frac{\partial V}{\partial X}\right)+\frac{\partial}{\partial Y}\left(\mu_r\frac{\partial V}{\partial Y}\right)\right)+\frac{\rho_{bf}}{\rho_{hnf}}S(\theta)V+PrRa\theta\frac{(\rho\beta)_{hnf}}{\rho_{hnf}\beta_{bf}} \tag{13}$$

Energy:

$$\frac{\partial\theta}{\partial Fo}+U\frac{\partial\theta}{\partial X}+V\frac{\partial\theta}{\partial Y}=\left(\frac{\partial}{\partial X}\left(\frac{\alpha_{hnf}(\varphi)}{\alpha_{l,bf}}\frac{\partial\theta}{\partial X}\right)+\frac{\partial}{\partial Y}\left(\frac{\alpha_{hnf}(\varphi)}{\alpha_{l,bf}}\frac{\partial\theta}{\partial Y}\right)\right)-\frac{(C_p)_{bf}}{(C_p)_{hnf}}\frac{1}{Ste}\frac{\partial\varphi(\theta)}{\partial Fo} \tag{14}$$

In the heat equation, the thermal diffusivity ratio can be evaluated as $\frac{\alpha_{hnf}(\varphi)}{\alpha_{l,bf}}=\frac{\varphi\alpha_{l,hnf}+(1-\varphi)\alpha_{s,hnf}}{\alpha_{l,bf}}$ which it can be written as $\frac{\alpha_{hnf}(\varphi)}{\alpha_{l,bf}}=\varphi\alpha r_l+(1-\varphi)\alpha r_s$ where $\alpha r_l=\frac{\alpha_{l,hnf}}{\alpha_{l,bf}}$ and. $\alpha r_s=\frac{\alpha_{l,hnf}}{\alpha_{l,bf}}$. Here, αr_l denotes the thermal diffusivity ratio of hybrid nanofluid and the base fluid for the liquid phase, and αr_s denotes the thermal diffusivity ratio of the hybrid nanofluid in the solid phase and the thermal diffusivity of the base fluid in the liquid phase. In the solid phase, the nanoparticles are trapped in the solid structure and they cannot freely move. In addition, the volume fraction of the nanoparticles is very low, and hence, they cannot affectively change the thermo-physical properties of the solid phase. Therefore, either it can be assumed that the thermal diffusivity of the solid hybrid nanofluid ($\alpha_{s,\ hnf}$) is equal to the thermal diffusivity of the solid base fluid ($\alpha_{s,\ bf}$), which as a result yields $\alpha_{s,\ bf}/\alpha_{l,\ bf}\approx 1$ or the thermal diffusivity of the solid hybrid nanofluid ($\alpha_{s,\ hnf}$) can be evaluated using the Maxwell model of nanofluids. It is worth noticing that the change in the thermal diffusivity of the liquid hybrid nanofluid ($\alpha_{l,\ hnf}$) due to the presence of hybrid nanoparticles is quite significant, and it should be taken into account.

Additionally, Eq. (19) is the non-dimensional form of the viscosity mentioned in Eq. (9) can be evaluated as:

$$\mu_r=(1+A_{mush}(1-\varphi)) \tag{15}$$

The relevant boundary conditions mentioned in Eq. (8) are transformed into the dimensionless form as follows:

On all externals walls of the cavity $\theta=0$ and $U=V=0$ (16a)

On the cylinder $\theta=1$ (16b)

In the above equations, *U* and *V* are the non-dimensional velocities in the X and Y directions, respectively. Additionally, *P* and θ represent the non-dimensional pressure and the non-dimensional temperature of the nanofluid, respectively. The subscripts *hnf*, *bf* and *p* specify the variables related to the nanofluid, the base fluid and the nanoparticles, respectively. The melt volume fraction as a function of θ can be written as:

$$\varphi(\theta)=\begin{cases}0 & \theta<0\\ \frac{\theta}{\Delta\theta} & 0<\theta<\Delta\theta\\ 1 & \theta>\Delta\theta\end{cases} \tag{17}$$

where $\Delta\theta=\frac{\Delta T}{T_h-T_f}$. The initial temperature in the non-dimensional form θ is equal to 0 in the cavity. According to the study of Zaraki et al. [31], the dynamic viscosity ratio and the thermal conductivity ratio can be measured using following relations:

$$\frac{\mu_{hnf}}{\mu_{bf}}=(1+N\nu\times\phi) \tag{18}$$

Table 1
The evaluated of *Nc* and *Nv* for different samples of hybrid nanofluids (cases 1-5) and single nano fluids (cases 6-11).

Case	Refs.	Base fluid	Temperature (°C)	Type	Size (nm)	Shape	Relative fraction	*Nc*	*Nv*
1	[32]	Water	–	Ag	25	Unspecific	0.5	20.3	6.2
				MgO	40	Unspecific	0.5		
2	[22]	Water	32	Al_2O_3	17	Spherical	0.9	9.2	33.29
				Cu	17	Spherical	0.1		
3	[33]	EG	30	ZnO	35–45	Spherical	0.5	6.68	–
				TiO_2	30	Spherical	0.5		
4	[34]	Water	60	Cu	55	Spherical	0.5(g)	4.03	–
				TiO_2	55	Spherical	5(g)		
5	[35]	EG	30	F-MWCNTs	ID = 3–5 OD = 5–15	Unknown	0.5	10.45	–
				Fe_3O_4	20–30	Spherical	0.5		
6	[36]	Water	15	TiO_2	21	Spherical	–	4.25	4.47
7	[36]	Water	25	TiO_2	21	Spherical	–	3.87	7.65
8	[36]	Water	25	ZnO	150	Rectangular	–	3.86	13.20
9	[37]	Water	25	MgO	40	Spherical	–	7.70	12.05
10	[38]	Kerosene	25	Al_2O_3	44	Spherical	–	14.1	15.62
11	[38]	Kerosene	25	Al_2O_3	21	Spherical	–	20.1	20.23

$$\frac{k_{hnf}}{k_{bf}} = (1 + Nc \times \phi) \tag{19}$$

where *Nv* and *Nc* represent the dynamic viscosity number and the thermal conductivity number, respectively, as discussed by Zaraki et al. [31]. Generally, *Nv* and *Nc* could be functions of the shape of nanoparticles, the size of nanoparticles, type of the base fluid, type of nanoparticles, and the method of preparation. According to Zaraki et al. [31], each synthesized nanofluid has a unique value of *Nv* and *Nc*, which could be obtained using a linear curve fit of the experimental data. Some values for *Nc* and *Nv* are represented in Table 1. For instance, Esfe et al. [32] prepared a Ag-MgO/water hybrid nanofluid combining 50% of Ag and 50% of MgO nanoparticles. They investigated the effects of the volume fraction of hybrid nanoparticles on the thermal conductivity and viscosity of a hybrid nanofluid. They reported the value of the thermal conductivity k_{hnf}/k_{bf} equal to approximately 1.2 for 3% volume fraction of hybrid nanoparticles and the value of the dynamic viscosity μ_{hnf}/μ_{bf} equal to approximately 1.4 for 2% of nanoparticles volume fraction. Additionally, Suresh et al. [23] reported 1.12 for the thermal conductivity and value close to 1.8 for the viscosity of Al_2O_3-Cu hybrid nanofluid prepared by 2% volume fraction of Al_2O_3-Cu hybrid nanoparticles. The values of the thermal conductivity parameter *Nc* and viscosity parameter *Nv* for different hybrid nanoparticles and single nanoparticles are presented in Table 1 which are obtained using the available experimental data in the literature for μ_{hnf}/μ_{bf} and k_{hnf}/k_{bf}.

Now, considering the liquid thermal diffusivity ratio ($\alpha r_l = \alpha_{l,\,hnf}/\alpha_{l,\,bf}$) as $\alpha_{l,\,hnf}/\alpha_{l,\,bf} = (k_{l,\,hnf}/k_{l,\,bf}) \times ((\rho C_p)_{l,bf}/(\rho C_p)_{l,hnf})$ and substituting $1 + Nv \times \phi$ for $k_{l,\,hnf}/k_{l,\,bf}$ from Eq. (23) gives:

$$\alpha r_l = (1 + Nv\phi)\frac{(\rho C_P)_{bf}}{(\rho C_P)_{hnf}} \tag{20}$$

3. Method of solution and validation

In order to solve the governing equations, the set of the nonlinear dimensionless partial differential equations, mentioned in Eqs. (11)–(14), and its relevant boundary conditions (16) are first transformed into a weak form and then have been solved by utilizing the Galerkin finite element method [39]. The continuity Eq. (11) is exploited as a constraint to satisfy the mass conservation by controlling the pressure distribution. The dimensionless pressure in the momentum equations is estimated by the continuity equation and the penalty parameter (χ) as described by [40] which can be written as follows:

$$P = \chi\left(\frac{\partial U}{\partial X} + \frac{\partial V}{\partial Y}\right) \tag{21}$$

Using Eq. (25), the momentum Eqs. (16) and (17) can be rewritten as follows:

$$\frac{\partial U}{\partial Fo} + U\frac{\partial U}{\partial X} + V\frac{\partial U}{\partial Y} = -\frac{\rho_{bf}}{\rho_{hnf}}\frac{\partial}{\partial X}\left(\chi\left(\frac{\partial U}{\partial X} + \frac{\partial V}{\partial Y}\right)\right) + \frac{\rho_{bf}}{\rho_{hnf}}\frac{\mu_{hnf}}{\mu_{bf}}Pr\left(\frac{\partial}{\partial X}\left(\mu_r\frac{\partial U}{\partial X}\right) + \frac{\partial}{\partial Y}\left(\mu_r\frac{\partial V}{\partial Y}\right)\right) + \frac{\rho_{bf}}{\rho_{hnf}}S(\theta)U \tag{22}$$

$$\frac{\partial V}{\partial Fo} + U\frac{\partial V}{\partial X} + V\frac{\partial V}{\partial Y} = -\frac{\rho_{bf}}{\rho_{hnf}}\frac{\partial}{\partial Y}\left(\chi\left(\frac{\partial U}{\partial X} + \frac{\partial V}{\partial Y}\right)\right) + \frac{\rho_{bf}}{\rho_{hnf}}\frac{\mu_{hnf}}{\mu_{bf}}Pr\left(\frac{\partial}{\partial X}\left(\mu_r\frac{\partial U}{\partial X}\right) + \frac{\partial}{\partial Y}\left(\mu_r\frac{\partial V}{\partial Y}\right)\right) + \frac{\rho_{bf}}{\rho_{hnf}}S(\theta)V + PrRa\theta\frac{(\rho\beta)_{hnf}}{\rho_{hnf}\beta_{bf}} \tag{23}$$

In Eqs. (22) and (23), the continuity Eq. (11) is satisfied for large values of the penalty parameter ($\chi = 10^7$) [40]. Now, the velocities *U* and *V* as well as the temperature, θ, can be expanded using a basis set $\{\xi_k\}_{k=1}^N$ in the domain interval of $-0.5 < X < 0.5$ and $0 < Y < 1$ as,

$$U \approx \sum_{k=1}^{N} U_k\xi(X,Y), V \approx \sum_{k=1}^{N} k_k\xi(X,Y), \theta \approx \sum_{k=1}^{N} \theta_k\xi(X,Y) \tag{24}$$

It is noteworthy that the basis function ζ for all of the three variables is the same which causes the total number of the nodes *N* to be equal to 3. By using the mentioned basis functions in Eq. (24), the nonlinear residual equations (R_i^N) of the governing Eqs. (11)–(14) can be rewritten as follows:

$$\begin{aligned} R_i^1 = {} & \sum_{k=1}^{N} U_k \int_\Omega \frac{\partial \xi_k}{\partial Fo}\xi_i dXdY \\ & + \sum_{k=1}^{N} U_k \int_\Omega \left[\left(\sum_{k=1}^{N} U_k\xi_k\right)\frac{\partial \xi_k}{\partial X} + \left(\sum_{k=1}^{N} V_k\xi_k\right)\frac{\partial \xi_k}{\partial Y}\right]\xi_i dXdY \\ & + \frac{\rho_{bf}}{\rho_{hnf}}\left(\sum_{k=1}^{N} U_k \int_\Omega \frac{\partial \xi_i}{\partial X}\left[(\chi)\frac{\partial \xi_k}{\partial X}dXdY\right] + \sum_{k=1}^{N} V_k \int_\Omega \frac{\partial \xi_i}{\partial X}\left[(\chi)\frac{\partial \xi_k}{\partial Y}dXdY\right]\right) \\ & + \frac{\rho_{bf}}{\rho_{hnf}}\frac{\mu_{hnf}}{\rho_{bf}}Pr\left[\sum_{k=1}^{N} U_k \int_\Omega \frac{\partial \xi_i}{\partial X}\left(\mu_r\frac{\partial \xi_k}{\partial X}dXdY\right)\right. \\ & \left. + \sum_{k=1}^{N} U_k \int_\Omega \frac{\partial \xi_i}{\partial Y}\left(\mu_r\frac{\partial \xi_k}{\partial Y}dXdY\right)\right] + \frac{\rho_{bf}}{\rho_{hnf}}S(\theta)\sum_{k=1}^{N}\int_\Omega\left(\sum_{k=1}^{N}(U_k\xi_k)\xi_i\right)dXdY \end{aligned} \tag{25}$$

$$R_i^2 = \sum_{k=1}^{N} V_k \int_\Omega \frac{\partial \xi_k}{\partial Fo}\xi_i dXdY + \sum_{k=1}^{N} V_k \int_\Omega \left[\left(\sum_{k=1}^{N} U_k\xi_k\right)\frac{\partial \xi_k}{\partial X} + \left(\sum_{k=1}^{N} V_k\xi_k\right)\frac{\partial \xi_k}{\partial Y}\right]\xi_i dXdY + \frac{\rho_{bf}}{\rho_{hnf}}\left(\sum_{k=1}^{N} U_k \int_\Omega \frac{\partial \xi_i}{\partial Y}\left[(\chi)\frac{\partial \xi_k}{\partial X}dXdY\right] + \sum_{k=1}^{N} V_k \int_\Omega \frac{\partial \xi_i}{\partial Y}\left[(\chi)\frac{\partial \xi_k}{\partial Y}dXdY\right]\right) + \frac{\rho_{bf}}{\rho_{hnf}}\frac{\mu_{hnf}}{\mu_{bf}}Pr\left[\sum_{k=1}^{N} V_k \int_\Omega \frac{\partial \xi_i}{\partial X}\left(\mu_r \frac{\partial \xi_k}{\partial X}dXdY\right) + \sum_{k=1}^{N} V_k \int_\Omega \frac{\partial \xi_i}{\partial Y}\left(\mu_r \frac{\partial \xi_k}{\partial Y}dXdY\right)\right] + \frac{(\rho\beta)_{hnf}}{\rho_{hnf}\beta_{bf}}RaPr\left[\int_\Omega \left(\sum_{k=1}^{N}\theta_k\xi_k\right)\xi_i dXdY\right] + \frac{\rho_{bf}}{\rho_{hnf}}S(\theta)\sum_{k=1}^{N}\int_\Omega \left(\sum_{k=1}^{N}(V_k\xi_k)\xi_i\right)dXdY \quad (26)$$

$$R_i^3 = \sum_{k=1}^{N} \theta_k \int_\Omega \frac{\partial \xi_k}{\partial Fo}\xi_i dXdY + \sum_{k=1}^{N} \theta_k \int_\Omega \left[\left(\sum_{k=1}^{N} U_k\xi_k\right)\frac{\partial \xi_k}{\partial X} + \left(\sum_{k=1}^{N} V_k\xi_k\right)\frac{\partial \xi_k}{\partial Y}\right]\xi_i dXdY + \frac{\alpha_{bf}}{\alpha_{hnf}}\left(\sum_{k=1}^{N} \theta_k \int_\Omega \frac{\partial \xi_i}{\partial X}\left[\alpha_r \frac{\partial \xi_k}{\partial X}dXdY\right] + \sum_{k=1}^{N} \theta_k \int_\Omega \frac{\partial \xi_i}{\partial Y}\left[\alpha_r \frac{\partial \xi_k}{\partial Y}dXdY\right]\right) + \frac{(C_p)_{bf}}{(C_p)_{hnf}}\frac{1}{Ste}\sum_{k=1}^{N} f_k \int_\Omega \frac{\partial \xi_k}{\partial Fo}\xi_i dXdY \quad (27)$$

3.1. Grid check

The grid independency of the solution is evaluated by using several grid sizes for the case in which $Nc = 20$, $Nv = 20$ $Pr = 50$, $Ra = 10^7$, $\alpha r_l = \alpha r_s = 1.0$, $Ste = 0.1$, $A_{mush} = 1.6 \times 10^6$, and $\phi = 2\%$. A supercomputer with 40 GB of memory and 20 CPU cores each of 2.2 GHz is utilized to obtain the results of the present study. Fig. 2 represents the variation of the liquid fraction versus the Fourier number for different grid sizes. The results indicate that 6000 quadrilateral elements can accurately estimate the results with a reasonable amount of time. In the case of 2000 quadrilateral elements, the time spent to obtain the results is 9 h and 48 min while in the case with 8000 quadrilateral elements took 1 day, 8 h and 23 min.

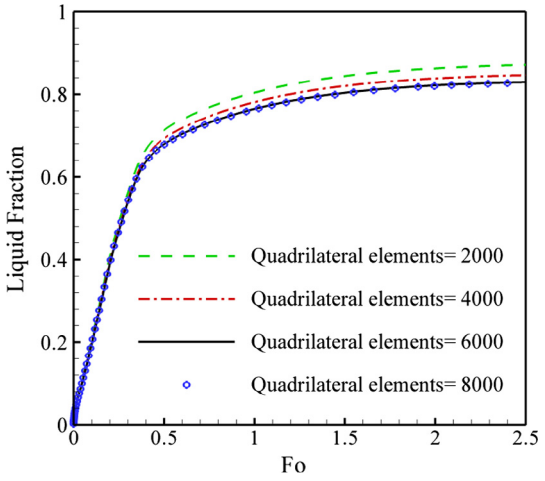

Fig. 2. The liquid fraction vs. Fourier number for various grid sizes.

3.2. Validation of the results

In order to examine the accuracy of the present study, several comparisons have been done. First, the results of the present study in the case of a rectangular enclosure without an inner cylinder are compared with the experimental results reported by Gau and Viskanta [41], and the numerical results available in the literature for the case in which the aspect ratio (height/width) of the rectangular cavity is equal to 0.714.

Gau and Viskanta [41] have studied the melting interface exploiting the pour-out method and the probing method. They assumed that the left wall is hot while the top and bottom walls are chosen to be insulated. In addition, the problem of the melting process of a phase-change material is numerically investigated by Kashani et al. [42], Khodadadi and Hosseinzadeh [43], Brent et al. [44], Joulin, et al. [45], Viswanta and Jaluria [46], Dessai and Vafai [47] and Tiari et al. [48] when $\phi = 0$ and $\alpha r_s = 1$. The comparison between the present study and the results in the literature is plotted in Fig. 3(a) and (b) which clearly shows an acceptable agreement. In the case of large Fourier numbers such as $Fo = 3.48$, a difference between the present results and the experimental results can be seen, which in previous studies, the authors

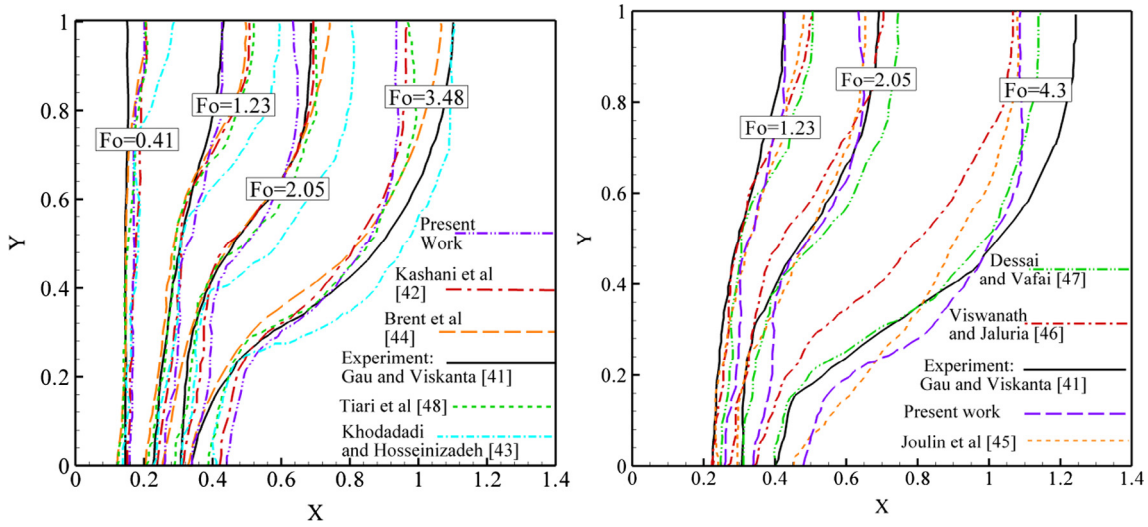

Fig. 3. A comparison between the present results and the experimental results of Gau and Viskanta [41] and numerical studies available in the literature (a) and (b): isothermal hot wall at the left and isothermal cooled wall at the right, keeping the bottom and top walls insulated, $Ra = 6 \times 10^5$, $Pr = 0.0216$.

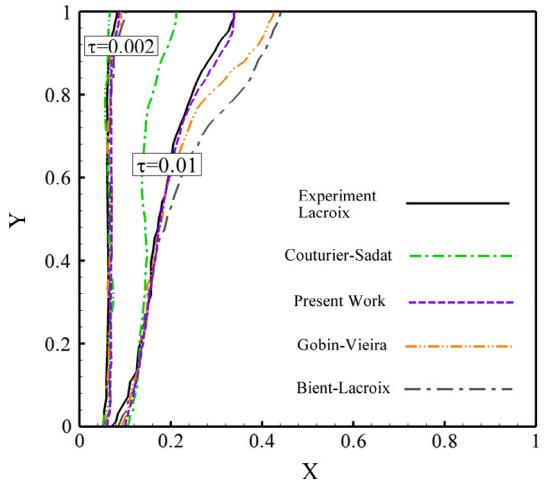

Fig. 4. A comparison between the results of the present study with the results of the benchmark study of Bertrand et al. [49] in the case when (a): $\tau = 2 \times 10^{-3}$ (b): $\tau = 1 \times 10^{-2}$, ($\tau = Fo \times Ste$).

have concluded that the difference could result from the method of measuring the melting interface in the experiments of Gau and Viskanta [41]. Because they evaluated the melting interface mechanically using a manual mechanical probe. In fact, in the case with large values of *Fo*, the solid-liquid interface of melting could be unstable which makes it hard to evaluate the exact shape of the interface.

In the second case, the results of the present finite element code are compared with the benchmark study of Bertrand et al. [49] when $Ra = 1 \times 10^7$, $Pr = 50$, $\phi = 0$ and $\alpha r_s = 1.0$, for which different authors have obtained the results of the melting interface for a square cavity. Fig. 4 clearly illustrates a good agreement between the results of the present study and the results of Bertrand et al. [49].

In the third case, the results of the present study are compared with the experimental study reported by Kumar et al. [50] for the melting of lead. They have investigated the melting of lead contained inside a stainless steel cuboid. In their study, a heater was located at one of the vertical side walls of the cavity to provide a constant heat flux, while the other walls were insulated. Using neutron radiography, they captured the photography of the solid-liquid interface movement, during the melting process of the lead. Table 2 provides the non-dimensional parameters used by Kumar et al. [50]. In their experiment, the temperature was linearly distributed before the melting started, because the heater increased the temperature on both sides of the cavity. Although, after the melting started, the temperature was higher at the right-hand side wall (the heater side) compared to the left-hand side wall. Due to the fact that the experiment by Kumar et al. [50] have been accomplished in the case in which heat flux is constant, the Rayleigh number, Stefan number, and the Prandtl number should be calculated, accordingly. Thus, the Rayleigh number and the Stefan number can be written as $Ra^* = g\beta q''_{cond} L_y^4/(k\alpha\nu)$ and $Ste^* = C_p\ q''_{cond} L_x^4/(kL)$, respectively.

The comparison between the results of the present study without the inner cylinder and the photography carried out by Kumar et al. [50] is shown in Fig. 5 in which both results represent a curved shape for the solid-liquid interface. In addition, both results indicate that the maximum and minimum depths happen at the top and bottom of the enclosure, respectively. Furthermore, increasing the values of *Fo* from 0.37 to 1.74 leads to increasing the depth of the solid-liquid interface predicted accurately by the present numerical results.

In the final case, the results of the Nusselt number of the present study are compared with the results reported by Hussein [51] for the case in which there is a hot cylinder inside a cavity filled with a pure molten fluid as shown in Fig. 6. The cylinder can be placed in different vertical locations inside the cavity where δ denotes the non-dimensional position of the center of the cylinder from the center of the cavity. Here, $\delta = 0$ indicates a cavity with a cylinder at its center the same as the present study. The Prandtl number in this comparison is considered equal to 0.71 similar to study of Hussein [51]. Obviously, for all of the chosen Rayleigh numbers, the results are in a complete agreement with the results reported by Hussein [51].

4. Results and discussion

In order to investigate the change phase heat transfer of nanofluids, a square cavity with the size of $H = 5$ cm, a cylinder with the radius R equal to 0.5 cm, which leads to the aspect ratio $R/H = 0.1$ is considered. The cavity is filled with Octadecane for which the thermophysical properties are presented in Table 3. The temperature at the surface of the inner cylinder T_h is equal to 40 °C and the temperature at the cold walls of the cavity is $T_c = 30$ °C. Thus, the corresponding non-dimensional parameters can be calculated as: $Pr = 50$, $Ste = 0.1$, $Ra = 1.25 \times 10^7$.

According to the experimental study by Esfe et al. [32] and the theoretical study by Zaraki et al. [31], the magnitudes of ρ_{bf}/ρ_{hnf}, $(\rho C_p)_{bf}/(\rho C_p)_{hnf}$, C_{bf}/C_{hnf} and $\rho_{hnf}\beta_{bf}/(\rho\beta)_{hnf}$ for most of nanofluids is close to unity. Likewise, in the present study, these values are considered equal to unity. In fact, only the dynamic viscosity and the thermal conductivity of the base fluid are significantly affected by the presence of the nanoparticles. Thus, by substituting $(\rho C_p)_{bf}/(\rho C_p)_{hnf} \approx 1$ and Eq. (19) in Eq. (20), the thermal diffusivity ratio α_{hnf}/α_{bf} can be simplified as:

$$\alpha r_l = \frac{k_{hnf}}{k_{bf}} \frac{(\rho C_P)_{bf}}{(\rho C_P)_{hnf}} = (1 + Nc \times \phi) \times (\approx 1) = 1 + Nc \times \phi \qquad (28)$$

The dynamic viscosity ratio and the thermal conductivity ratio are calculated utilizing Eqs. (22) and (23). As a results, the non-dimensional parameters in the present study can be summarized as $Pr = 50$, $Ste = 0.1$, $\alpha r_s = 1.0$, $Ra = 1.25 \times 10^7$. The mentioned non-dimensional values are utilized in order to obtain the results of this section, otherwise, the values of the non-dimensional parameters will be stated. The thermal diffusivity ratio of the liquid hybrid nanofluid to the thermal diffusivity of the base fluid (αr_l) and the dynamic viscosity ratio (μ_{hnf}/μ_{bf}) are respectively a function of the thermal conductivity number (Nc) and the dynamic viscosity number (Nv), and they can be evaluated using Eq. (28) and Eq. (18), accordingly. The thermal conductivity number (Nc) and the dynamic viscosity number (Nv) have been summarized for some typical nanofluids and hybrid nanofluids in Table 1.

Table 2
Input provided for one case in the simulation by Kumar et al. [50].

Heater input (right side)	Prandtl number	Stefan number	Rayleigh number	Temp at left side (K)	Temp at right side (K)
16.3 kW/m^2	0.0236	0.4	1.4×10^7	555	599

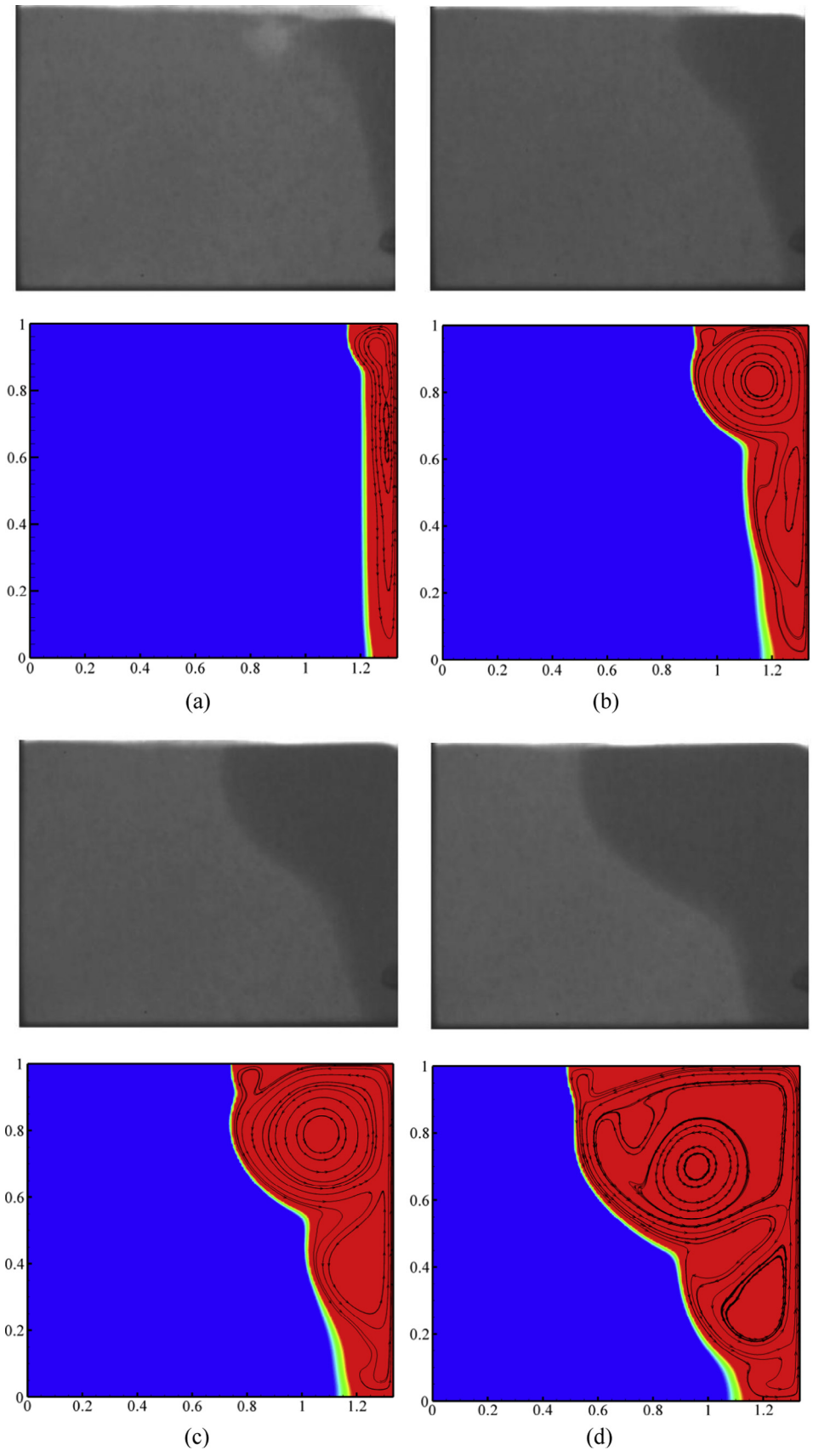

Fig. 5. The result of benchmark experimental of Kumar et al. [50] and the results of present study when (a) *Fo* = 0.37, (b) *Fo* = 0.73, (c) *Fo* = 1.10, (d) *Fo* = 1.47.

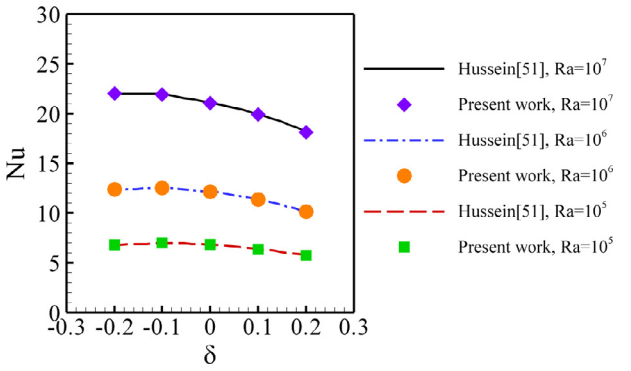

Fig. 6. The results of the present study for the Nusselt number and the results of Hussein [51], when $Pr = 0.71$ and $R/H = 0.2$.

Table 3
Thermophysical properties of Octadecane.

Property	*Symbol*	Value	Unit
Density (Solid/Liquid)	ρ	800	(kg/m^3)
Thermal expansion coefficient	β	2×10^{-3}	(1/K)
Fusion temperature	T_f	303.16	(K)
Thermal conductivity (Solid/Liquid)	k	0.2	(W/m K)
Latent heat of fusion	L	1.25×10^{-5}	(J/kg)
Specific heat capacity (Solid/Liquid)	C	1250	(J/kg K)
Dynamic viscosity	μ	8×10^{-3}	(kg/m s)

Fig. 7 depicts as the Fourier number increases, the liquids interface further moves into the solid regions. In fact, the Fourier number is a dimensionless parameter representing the ratio between the conduction rate and the thermal energy storage rate through time. As the Fourier number increases, the depth of the solid-liquid interface remarkably increases.

Fig. 7 illustrates the streamlines and the isotherms for different values of the Fourier number, the conductivity parameter, the viscosity parameter and the volume fraction of nanoparticles. As discussed, different values of Nc and Nv can represent various types of regular nanofluids or hybrid nanofluids. For example if $Nc \approx 4$, then according to the study of Madhesh et al. [34], the type of hybrid nanoparticles are Cu/TiO_2 and their sizes is 55 nm. The case of $Nc \approx 20$ corresponds to a Ag-Mgo hybrid nanofluid with Ag nanoparticles with a size of 25 nm and Mgo nanoparticles with a size of 40 nm [32].

As the values of ϕ, Nc and Nv increase, Fig. 7 illustrates that the depth of the solid-liquid interface augments for a constant value of the Fourier number. This is due to the fact that adding the hybrid or single nanoparticles increases the base fluid viscosity and thermal conductivity. Adding the hybrid or single nanoparticles affects the thermal conductivity of the base fluid which leads to an augmentation in the strength of the heat conduction throughout the NEPCM in the cavity. In the beginning of the melting process, i.e. small values of the Fourier number, the flow motion is weak and most parts of the cavity are filled with the solid phase, and hence,

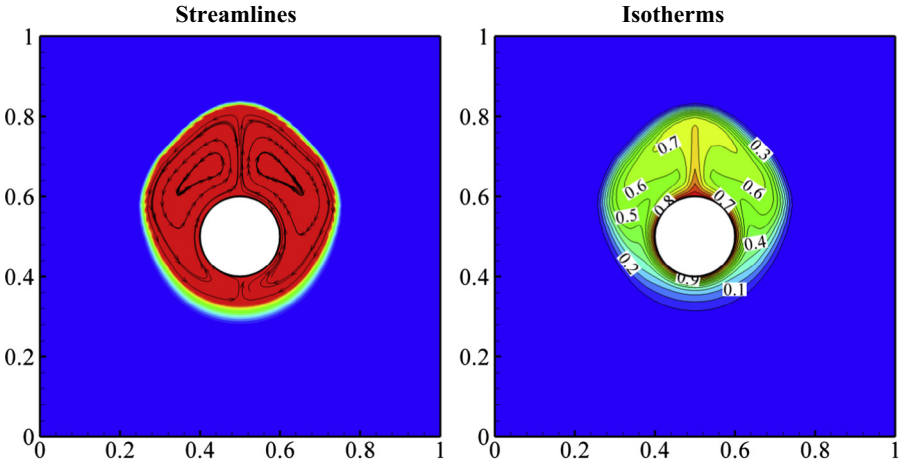

Fig. 7. Streamlines and isotherms, when (a) $F_o = 0.1$, (b): $F_o = 0.3$, (c) $F_o = 1$.

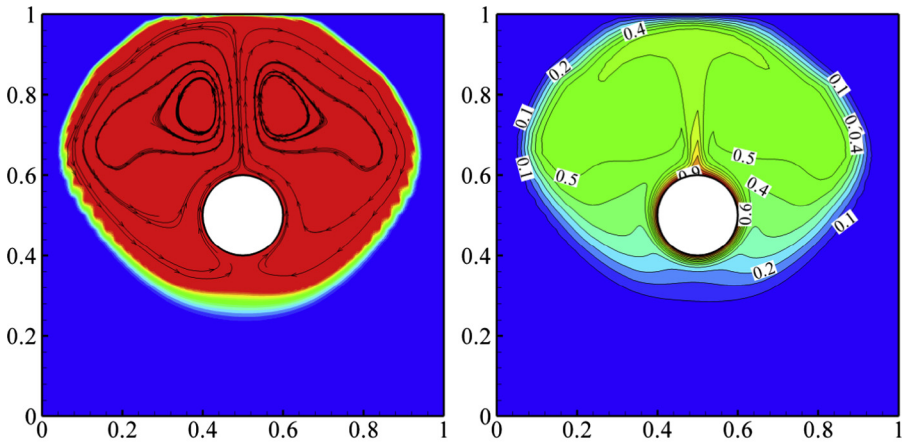

(b-1): ϕ=0%, Nc=Nv=0

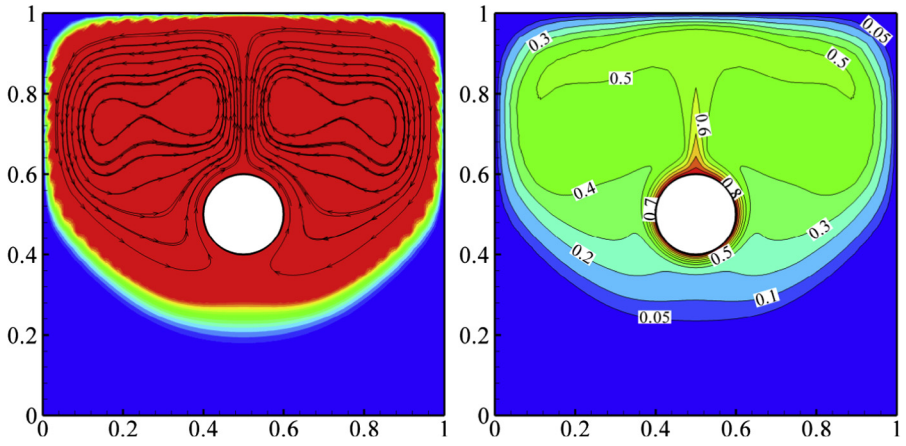

(b-2): ϕ=5%, Nc=20, Nv=4

Fig. 7 (*continued*)

the dominant mechanism of heat transfer is the diffusion mechanism due to a higher thermal conductivity of the hybrid nanofluid. As the presence of nanoparticles enhances the thermal conductivity of the PCM, the melting space around the cylinder in the case of the hybrid nanofluid is higher than that of the pure base fluid. These results can be seen by a visual comparison between the results of Fig. 7-a-1 and a-2.

After a while, the melting process advances (higher values of the Fourier number) and more parts of the cavity are transformed from the solid phase to the liquid phase. In this case, the convective heat transfer regime due to the buoyancy forces gets stronger. The buoyancy flows tend to move the hot fluid in the upward direction and towards the top cold walls or the cold solid regions above the cylinder. As the hot liquid reaches the cold solid phase above the cylinder, the melting process accelerates and the solid phase changes into the fresh cold liquid phase. This cold liquid is denser than its surrounding hot liquid and tends to move downward due to buoyancy forces. As a result, the cold fresh liquid moves downward through the regions on the right and left hand sides of the cylinder. Indeed, the upward direction of the convective flow takes place right above the cylinder, and the downward direction takes place in the right and left hand sides of the cylinder. In the case of the hybrid nanofluid, in which the diffusion mechanism is stronger than that of the pure base fluid, the liquid regions are bigger. As a result, the convective circulation areas in the case of a hybrid nanofluid are larger than those of a pure base fluid.

Figs. 8–10 illustrate the effects of the nanoparticles volume fraction and the Fourier number on the solid-liquid interface. Fig. 8 indicates that for small values of the thermal conductivity parameter, increasing the nanoparticles volume fraction does not have a significant impact on the melting front. In contrast, it can be seen from Figs. 9 and 10 that for large values of the thermal conductivity parameter. According to the study of Chandrasekar et al. [38], the case of Nc = 20 and Nv = 20 corresponds to 21 nm Al_2O_3 nanoparticles and the case of Nc = 4 and Nv = 4 corresponds to 21 nm TiO_2 nanoparticles [36].

Figs. 9 and 10 show that the melting front is remarkably affected by the volume fraction of nanoparticles. This is due to the fact that a larger thermal conductivity parameter causes strong conduction in the boundary layer which leads to an increase in the depth of the solid-liquid interface. It is worth mentioning that the boundary layer thickness above the cylinder is much larger than the one below it which is caused by the buoyancy force.

The effects of the thermal conductivity and viscosity parameters on the liquid fraction versus the Fourier number are shown in Figs. 11–13 for different values of the nanoparticles volume fraction. According to the study of Madhesh et al. [34], for Nc = 4, the type of hybrid nanoparticles are Cu/TiO_2 and their sizes are equal

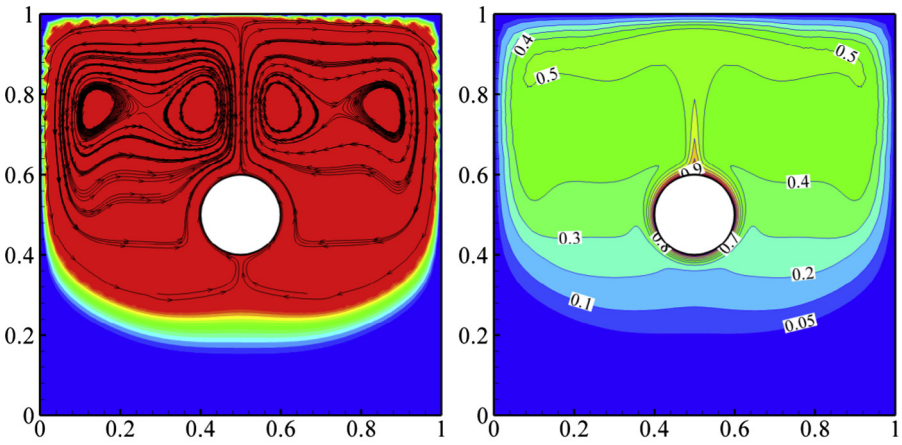

(c-1): ϕ=0%, Nc=Nv=0

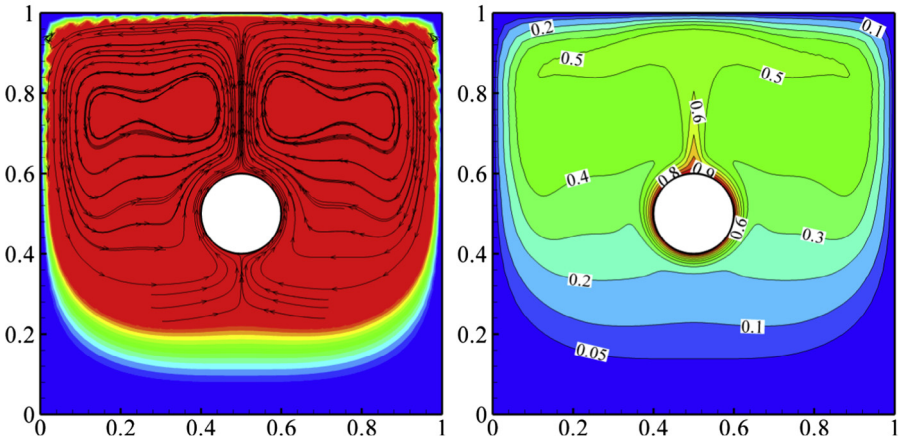

(c-2): ϕ=5%, Nc=20, Nv=4

Fig. 7 (*continued*)

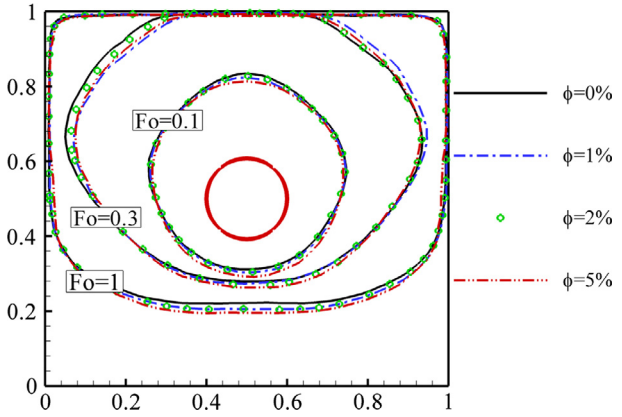

Fig. 8. The melting front for Nc = 4, Nv = 20.

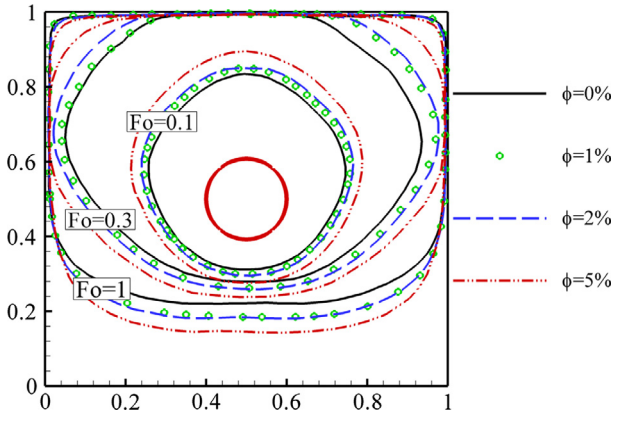

Fig. 9. The melting front for Nc = 20, Nv = 20.

to 55 nm. According to the study of Chandrasekar et al. [38], the type of single nanoparticles is Al_2O_3 within the size of 21 nm. Figs. 12 and 13 clearly indicate that for a viscosity parameter equals to 20, the liquid fraction significantly increases as the conductivity parameter increases from 4 to 20 for all considered values of the Fourier number. Comparing this phenomenon for different values of the nanoparticles volume fraction indicates that for larger values of the nanoparticles volume fractions, as the thermal conductivity parameter increases, the change in the liquid fraction is much larger than for the small values of the nanoparticles volume fractions. In contrast, for constant values of the thermal conductivity parameter, as the viscosity parameter increases, the liquid fraction does not change significantly. Moreover, it can be seen that as the Fourier number increases from 0 to 0.5, the liquid fraction significantly increases for all the values of the nanoparticles volume fraction, and the thermal conductivity and viscosity parameters. However, further increase in the Fourier number does not have substantial effects on the liquid fraction.

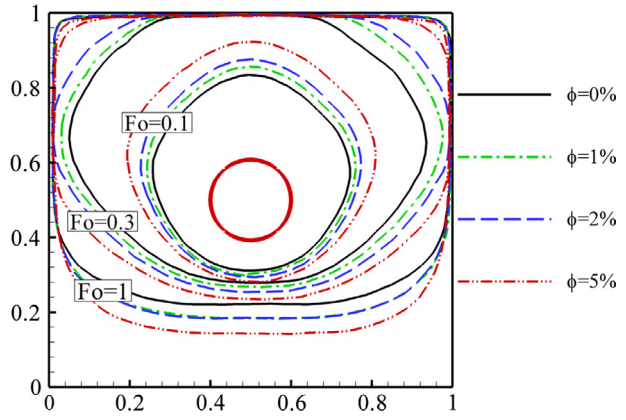

Fig. 10. The melting front for $Nc = 20$, $Nv = 4$.

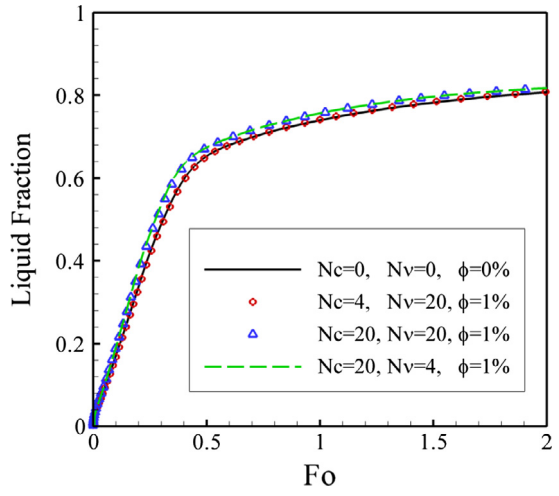

Fig. 11. Effect of $\phi = 1\%$ volume fraction of nanoparticles on liquid fraction for different Nc and Nv.

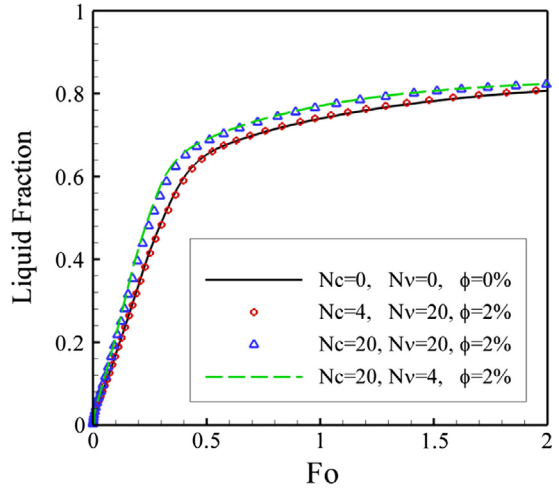

Fig. 12. Effect of $\phi = 2\%$ volume fraction of nanoparticles on liquid fraction for different Nc and Nv.

The hybrid nanofluids which have Nc much greater than Nv or say equivalent values, are expected to melt faster than those having $Nc \gg Nv$. Thus, the hybrid nanoparticles configuration of Esfe et al. [32], which uses Ag-MgO nanoparticles dispersed in water

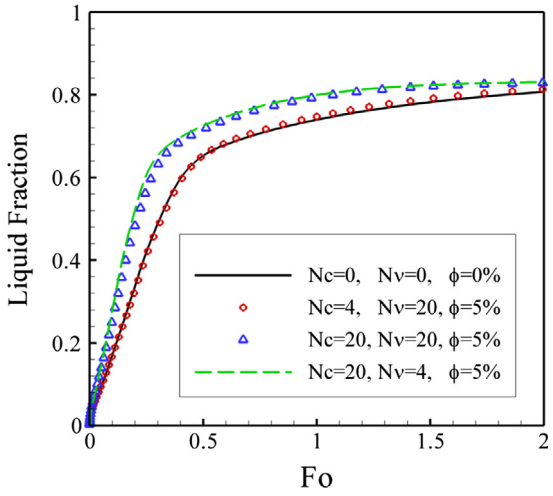

Fig. 13. Effect of $\phi = 5\%$ volume fraction of nanoparticles on liquid fraction for different Nc and Nv.

can be considered as having a great chance in accelerating the melting process.

5. Conclusion

The melting process of a nano-enhanced phase-change material in a square cavity in the presence of a hot inner cylinder is investigated in this paper. The governing partial differential equations are first transformed into a dimensionless form and then solved numerically using the Galerkin finite element method using 6000 quadrilateral elements. The Prandtl number, the Stefan number, the Rayleigh number, and the thermal diffusivity ratio are kept constant and equal to 50, 0.1, 1.25×10^7 and 1, respectively, while the effects of the other parameters such as the volume fraction of nanoparticles, the Fourier number, the thermal conductivity number, and the viscosity parameter are investigated. It is found that the solid-liquid interface is substantially affected by the volume fraction of nanoparticles for large values of the thermal conductivity. However, as the viscosity parameter changes, the melting front and the liquid fraction do not change significantly. Likewise, the liquid fraction augments as the thermal conductivity parameter increases. The augmentation in the values of the liquid fraction is much more noticeable for larger values of the nanoparticles volume fractions. Furthermore, the Fourier number has a remarkable impact on both the melting front and the liquid fraction. For the values of the Fourier number between 0 and 0.5, the rate of the melting is much larger compared to the larger values of the Fourier number.

In the present study, the single/hybrid nanofluids with a Newtonian behavior are analyzed. However, there are also nanofluids and hybrid nanofluids with non-Newtonian behaviors which could be subject of future studies.

Acknowledgements

This research is financially supported by Dezful Branch, Islamic Azad University, Dezful, Iran. The authors like to express their appreciation to Sheikh Bahaei National High-Performance Computing Center (SBNHPCC) for providing computational resources, supported by the scientific and technological department of the presidential office and Isfahan University of Technology (IUT). The authors are also thankful to Iran Nanotechnology Initiative Council (INIC) and National Iranian Drilling Company (NIDC) for the financial support of the present study.

References

[1] G. Cesini, M. Paroncini, G. Cortella, M. Manzan, Natural convection from a horizontal cylinder in a rectangular cavity, Int. J. Heat Mass Transf. 42 (1999) 1801–1811.
[2] H.S. Yoon, M.Y. Ha, B.S. Kim, D.H. Yu, Effect of the position of a circular cylinder in a square enclosure on natural convection at Rayleigh number of 107, Phys. Fluids 21 (2009), 047101–047101.
[3] Z. Huang, W. Zhang, G. Xi, Natural convection in square enclosure induced by inner circular cylinder with time-periodic pulsating temperature, Int. J. Heat Mass Transf. 82 (2015) 16–25.
[4] P. Zhang, X. Zhang, J. Deng, L. Song, A numerical study of natural convection in an inclined square enclosure with an elliptic cylinder using variational multiscale element free Galerkin method, Int. J. Heat Mass Transf. 99 (2016) 721–737.
[5] S. Gharbi, S. Harmand, S.B. Jabrallah, Experimental comparison between different configurations of PCM based heat sinks for cooling electronic components, Appl. Therm. Eng. 87 (2015) 454–462.
[6] F. Agyenim, The use of enhanced heat transfer phase change materials (PCM) to improve the coefficient of performance (COP) of solar powered LiBr/H_2O absorption cooling systems, Renew. Energy 87 (2016) 229–239.
[7] F. Tan, C. Tso, Cooling of mobile electronic devices using phase change materials, Appl. Therm. Eng. 24 (2004) 159–169.
[8] Y.-C. Weng, H.-P. Cho, C.-C. Chang, S.-L. Chen, Heat pipe with PCM for electronic cooling, Appl. Energy 88 (2011) 1825–1833.
[9] Z. Ling, Z. Zhang, G. Shi, X. Fang, L. Wang, X. Gao, Y. Fang, T. Xu, S. Wang, X. Liu, Review on thermal management systems using phase change materials for electronic components, Li-ion batteries and photovoltaic modules, Renew. Sustain. Energy Rev. 31 (2014) 427–438.
[10] M.A. Sharif, A. Al-Abidi, S. Mat, K. Sopian, M.H. Ruslan, M.Y. Sulaiman, M. Rosli, Review of the application of phase change material for heating and domestic hot water systems, Renew. Sustain. Energy Rev. 42 (2015) 557–568.
[11] V.G. Gude, Energy storage for desalination processes powered by renewable energy and waste heat sources, Appl. Energy 137 (2015) 877–898.
[12] J. Zeng, L. Sun, F. Xu, Z. Tan, Z. Zhang, J. Zhang, T. Zhang, Study of a PCM based energy storage system containing Ag nanoparticles, J. Therm. Anal. Calorim. 87 (2006) 371–375.
[13] Y.-D. Liu, Y.-G. Zhou, M.-W. Tong, X.-S. Zhou, Experimental study of thermal conductivity and phase change performance of nanofluids PCMs, Microfluid. Nanofluid. 7 (2009) 579–584.
[14] S. Wu, D. Zhu, X. Zhang, J. Huang, Preparation and melting/freezing characteristics of Cu/paraffin nanofluid as phase-change material (PCM), Energy Fuels 24 (2010) 1894–1898.
[15] S. Harikrishnan, S. Kalaiselvam, Preparation and thermal characteristics of CuO–oleic acid nanofluids as a phase change material, Thermochim. Acta 533 (2012) 46–55.
[16] A. Malvandi, S. Moshizi, D. Ganji, Two-component heterogeneous mixed convection of alumina/water nanofluid in microchannels with heat source/sink, Adv. Powder Technol. 27 (2016) 245–254.
[17] A. Malvandi, A. Ghasemi, D. Ganji, I. Pop, Effects of nanoparticles migration on heat transfer enhancement at film condensation of nanofluids over a vertical cylinder, Adv. Powder Technol. 27 (2016) 1941–1948.
[18] A. Malvandi, S. Heysiattalab, D. Ganji, Effects of magnetic field strength and direction on anisotropic thermal conductivity of ferrofluids (magnetic nanofluids) at filmwise condensation over a vertical cylinder, Adv. Powder Technol. 27 (2016) 1539–1546.
[19] H. Shahmohamadi, M.M. Rashidi, VIM solution of squeezing MHD nanofluid flow in a rotating channel with lower stretching porous surface, Adv. Powder Technol. 27 (2016) 171–178.
[20] N. Makulati, A. Kasaeipoor, M. Rashidi, Numerical study of natural convection of a water–alumina nanofluid in inclined C-shaped enclosures under the effect of magnetic field, Adv. Powder Technol. 27 (2016) 661–672.
[21] M.H. Abolbashari, N. Freidoonimehr, F. Nazari, M.M. Rashidi, Analytical modeling of entropy generation for Casson nano-fluid flow induced by a stretching surface, Adv. Powder Technol. 26 (2015) 542–552.
[22] S. Suresh, K. Venkitaraj, P. Selvakumar, M. Chandrasekar, Synthesis of Al_2O_3–Cu/water hybrid nanofluids using two step method and its thermo physical properties, Colloids Surf., A 388 (2011) 41–48.
[23] S. Suresh, K. Venkitaraj, P. Selvakumar, M. Chandrasekar, Effect of Al_2O_3–Cu/water hybrid nanofluid in heat transfer, Exp. Thermal Fluid Sci. 38 (2012) 54–60.
[24] H. Yarmand, S. Gharehkhani, G. Ahmadi, S.F.S. Shirazi, S. Baradaran, E. Montazer, M.N.M. Zubir, M.S. Alehashem, S. Kazi, M. Dahari, Graphene nanoplatelets–silver hybrid nanofluids for enhanced heat transfer, Energy Convers. Manage. 100 (2015) 419–428.
[25] B. Takabi, S. Salehi, Augmentation of the heat transfer performance of a sinusoidal corrugated enclosure by employing hybrid nanofluid, Adv. Mech. Eng. 6 (2014) 147059.
[26] B. Takabi, H. Shokouhmand, Effects of Al_2O_3–Cu/water hybrid nanofluid on heat transfer and flow characteristics in turbulent regime, Int. J. Mod. Phys. C 26 (2015) 1550047.
[27] S.S.U. Devi, S.A. Devi, Numerical investigation of three-dimensional hybrid Cu–Al_2O_3/water nanofluid flow over a stretching sheet with effecting Lorentz force subject to Newtonian heating, Can. J. Phys. 94 (2016) 490–496.
[28] M. Asadi, A. Asadi, Dynamic viscosity of MWCNT/ZnO–engine oil hybrid nanofluid: An experimental investigation and new correlation in different temperatures and solid concentrations, Int. Commun. Heat Mass Transfer 76 (2016) 41–45.
[29] B. Takabi, A.M. Gheitaghy, P. Tazraei, Hybrid water-based suspension of Al_2O_3 and Cu nanoparticles on Laminar convection effectiveness, J. Thermophys. Heat Transfer (2016) 1–10.
[30] J. Buongiorno, Convective transport in nanofluids, J. Heat Transfer 128 (2006) 240–250.
[31] A. Zaraki, M. Ghalambaz, A.J. Chamkha, M. Ghalambaz, D. De Rossi, Theoretical analysis of natural convection boundary layer heat and mass transfer of nanofluids: effects of size, shape and type of nanoparticles, type of base fluid and working temperature, Adv. Powder Technol. 26 (2015) 935–946.
[32] M.H. Esfe, A.A.A. Arani, M. Rezaie, W.-M. Yan, A. Karimipour, Experimental determination of thermal conductivity and dynamic viscosity of Ag–MgO/water hybrid nanofluid, Int. Commun. Heat Mass Transfer 66 (2015) 189–195.
[33] D. Toghraie, V.A. Chaharsoghi, M. Afrand, Measurement of thermal conductivity of ZnO–TiO_2/EG hybrid nanofluid, J. Therm. Anal. Calorim. (2016) 1–9.
[34] D. Madhesh, R. Parameshwaran, S. Kalaiselvam, Experimental investigation on convective heat transfer and rheological characteristics of Cu–TiO_2 hybrid nanofluids, Exp. Thermal Fluid Sci. 52 (2014) 104–115.
[35] S.S. Harandi, A. Karimipour, M. Afrand, M. Akbari, A. D'Orazio, An experimental study on thermal conductivity of F-MWCNTs–Fe_3O_4/EG hybrid nanofluid: effects of temperature and concentration, Int. Commun. Heat Mass Transfer 76 (2016) 171–177.
[36] W. Duangthongsuk, S. Wongwises, Measurement of temperature-dependent thermal conductivity and viscosity of TiO_2-water nanofluids, Exp. Thermal Fluid Sci. 33 (2009) 706–714.
[37] M.H. Esfe, S. Saedodin, M. Mahmoodi, Experimental studies on the convective heat transfer performance and thermophysical properties of MgO–water nanofluid under turbulent flow, Exp. Thermal Fluid Sci. 52 (2014) 68–78.
[38] M. Chandrasekar, S. Suresh, A.C. Bose, Experimental investigations and theoretical determination of thermal conductivity and viscosity of Al_2O_3/water nanofluid, Exp. Thermal Fluid Sci. 34 (2010) 210–216.
[39] O.C. Zienkiewicz, R.L. Taylor, P. Nithiarasu, The Finite Element Method for Fluid Dynamics, 2013.
[40] J.N. Reddy, An introduction to the Finite Element Method, McGraw-Hill, New York, 1993.
[41] C. Gau, R. Viskanta, Melting and solidification of a pure metal on a vertical wall, J. Heat Transfer 108 (1986) 174–181.
[42] S. Kashani, A. Ranjbar, M. Abdollahzadeh, S. Sebti, Solidification of nano-enhanced phase change material (NEPCM) in a wavy cavity, Heat Mass Transf. 48 (2012) 1155–1166.
[43] J. Khodadadi, S. Hosseinizadeh, Nanoparticle-enhanced phase change materials (NEPCM) with great potential for improved thermal energy storage, Int. Commun. Heat Mass Transfer 34 (2007) 534–543.
[44] A. Brent, V. Voller, K.t.J. Reid, Enthalpy-porosity technique for modeling convection-diffusion phase change: application to the melting of a pure metal, Numer. Heat Transf., A Appl. 13 (1988) 297–318.
[45] A. Joulin, Z. Younsi, L. Zalewski, D.R. Rousse, S. Lassue, A numerical study of the melting of phase change material heated from a vertical wall of a rectangular enclosure, Int. J. Comput. Fluid Dyn. 23 (2009) 553–566.
[46] R. Viswanath, Y. Jaluria, A comparison of different solution methodologies for melting and solidification problems in enclosures, Numer. Heat Transf., B Fundamentals 24 (1993) 77–105.
[47] C. Desai, K. Vafai, A unified examination of the melting process within a two-dimensional rectangular cavity, J. Heat Transfer 115 (1993) 1072–1075.
[48] S. Tiari, S. Qiu, M. Mahdavi, Numerical study of finned heat pipe-assisted latent heat thermal energy storage system, Bull. Am. Phys. Soc. 59 (2014).
[49] O. Bertrand, B. Binet, H. Combeau, S. Couturier, Y. Delannoy, D. Gobin, M. Lacroix, P. Le Quéré, M. Médale, J. Mencinger, Melting driven by natural convection A comparison exercise: first results, Int. J. Therm. Sci. 38 (1999) 5–26.
[50] L. Kumar, B. Manjunath, R. Patel, S. Markandeya, R. Agrawal, A. Agrawal, Y. Kashyap, P. Sarkar, A. Sinha, K. Iyer, Experimental investigations on melting of lead in a cuboid with constant heat flux boundary condition using thermal neutron radiography, Int. J. Therm. Sci. 61 (2012) 15–27.
[51] A.K. Hussein, Computational analysis of natural convection in a parallelogrammic cavity with a hot concentric circular cylinder moving at different vertical locations, Int. Commun. Heat Mass Transfer 46 (2013) 126–133.